*Document Version*
Peer reviewed version

*Citation for published version (APA):*
Zhang, Q., Li, Y. J., Wen, H. F., Adachi, Y., Miyazaki, M., Sugawara, Y., Xu, R., Cheng, Z. H., Brindiar, J., Kantorovitch, L., & Štich, I. (2018). Measurement and Manipulation of the Charge State of Adsorbed Oxygen Adatom on Rutile TiO2(110)- 1×1 Surface by nc-AFM and KPFM. *Journal of the American Chemical Society*, *46*, 15668-15674. https://doi.org/10.1021/jacs.8b07745

# Measurement and Manipulation of the Charge State of Adsorbed Oxygen Adatom on Rutile TiO$_2$(110)-1×1 Surface by nc-AFM and KPFM

Quanzhen Zhang[†], Yan Jun Li[†*], Huan Fei Wen[†], Yuuki Adachi[†], Masato Miyazaki[†], Yasuhiro Sugawara[†], Rui Xu[‡], Zhi Hai Cheng[‡], Ján Brndiar[$], Lev Kantorovich[§], and Ivan Štich[$,°]

[†] Department of Applied Physics, Graduate School of Engineering, Osaka University, 2-1 Yamadaoka, Suita, Osaka 565-0871, Japan
[‡] CAS Key Laboratory of Standardization and Measurement for Nanotechnology, CAS Center for Excellence in Nanoscience, National Center for Nanoscience and Technology, Beijing 100190, P. R. China
[$] Center for Computational Materials Science, Institute of Physics, Slovak Academy of Sciences, 84511 Bratislava, Slovakia
[§] Department of Physics, King's College London, The Strand, London, WC2R 2LS, United Kingdom
[°] Institute of Informatics, Slovak Academy of Sciences, 845 07 Bratislava, Slovakia

*Oxygen adatom, charge state, noncontact atomic force microscopy (nc-AFM), Kelvin probe force microscopy (KPFM), tip-sample distance, tip-induced electric field, density functional theory (DFT).*

**ABSTRACT:** For the first time, the charge states of adsorbed oxygen adatoms on rutile TiO$_2$(110)-1×1 surface are successfully measured and deliberately manipulated by a combination of noncontact atomic force microscopy and Kelvin probe force microscopy at 78 K in ultrahigh vacuum and interpreted by extensive density functional theory modeling. Several kinds of single and double oxygen adatom species are clearly distinguished and assigned to three different charge states: $O_{ad}^-$/$2O_{ad}^-$, $O_{ad}^{2-}$/$2O_{ad}^{2-}$ and $O_{ad}^-$-$O_{ad}^{2-}$, i.e. to formal charges of either one or two electrons per atom. Due to the strong atomic-scale image contrast, these states are clearly resolved. The observations are supported by measurements of the short-range force and local contact potential difference as a function of tip-sample distance, as well as simulations. Comparison with the simulations suggests subatomic resolution by allowing to resolve the rotated oxygen $p$ orbitals. In addition, we manage to switch reversibly the charge states of the oxygen adatoms, between the $O_{ad}^-$ and $O_{ad}^{2-}$ states, both individually and next to another oxygen, by modulating the frequency shift at constant positive voltage during both charging and discharging processes, i.e. by the tip-induced electric field of one orientation. This work provides a novel route for the investigation of the charge state of the adsorbates and opens up novel prospects for studying transition metal oxide based catalytic reactions.

## INTRODUCTION

The charge states of individual surface-supported adsorbates have dramatic effect on their physical and chemical properties[1,2]. In this respect, enormous experimental progress has been made, in combination with theoretical modeling, in detection and control of the charge state of the adsorbates at the ultimate spatial limit. For example, the charge state of metal adatoms[2-6], single molecule[7-12], quantum dots[13-15] as well as dopants[16-18] has been successfully measured and manipulated by means of scanning probe microscopy in a controlled manner. Among these studies, noncontact atomic force microscopy (nc-AFM), with high sensitivity at the atomic level and without limitation of having the conducting substrate, plays an important role in revolutionizing the investigation of the charge state of adsorbates. Specifically, scanning tunneling microscopy (STM) studies of charge state of adsorbates are complicated by tunneling currents into conducting substrate, which can easily result in unintended switching of the imaged charge during measurement. In contrast, nc-AFM completely avoids the unintended spurious charge manipulation due to its force modulation mechanism. In addition to the capability of characterizing surface structural and electronic properties with atomic resolution[19,20], nc-AFM has recently been used as a powerful tool for measuring and controlling the charge state of the adsorbates, as well as for directly manipulating the adsorbed atoms, such as measuring and switching the charge state of adsorbed metal adatoms through voltage pulse[3], charging and discharging the adsorbed molecules using Kelvin probe force spectroscopy (KPFS) with single-electron sensitivity[21,22], and manipulating adsorbed atoms laterally and vertically[23,24].

Catalytic reactions on the oxygen-rich titanium dioxide (O−TiO$_2$) surface, a prototypical catalytic model system, have recently captured extensive interest with a host of experimental and theoretical studies focusing on adsorption and dissociation behavior of adsorbed oxygen species[25-38]. Usually the adsorbed oxygen enters the catalytic reaction in a form of a single oxygen adatom ($O_{ad}$)[25,28-31,33,34,38], and the activation of the adsorbed $O_{ad}$ is a key factor toward the catalytic reactions, which considerably depends on its charge state[26,31-34,39,40]. Up to now, the charge state of adsorbed oxygen molecules has been clearly identified[21,39-44] and assigned to neutral O$_2$, as well as charged (O$_2$)$^-$ and (O$_2$)$^{2-}$ . In addition, the charge state transition of the adsorbed oxygen molecules between O$_2$ and (O$_2$)$^-$ has been demonstrated with a combination of nc-AFM and STM[21]. However, despite its importance to catalytic reactions, the possible charge states of adsorbed $O_{ad}$ have been studied to much lesser extent, both experimentally and theoretically.

It is well known that the anatase TiO$_2$ surface is free of polaronic defects, which provide the charge necessary to dissociate the molecular species[21]. The situation is different for rutile TiO$_2$, see Figure 1, which, in its stoichiometric form, is an inert insulator with a band gap of 3.03 eV[45]. Traditional sample preparation techniques in vacuum (Ar ion sputtering and thermal annealing) result in a partially reduced n-type semiconductor with point defects, including oxygen vacancies (O$_v$) and Ti interstitials (Ti$_{int}$), both on the surface and in the near-surface region, respectively. Hence, here we focus on the rutile TiO$_2$(110)-1×1 surface where the abundant defects leave the oxygen species dissociated. In fact, as shown below, the polaronic defects and

the charge they carry on the rutile $TiO_2$ surface are responsible for many of the unusual properties we report.
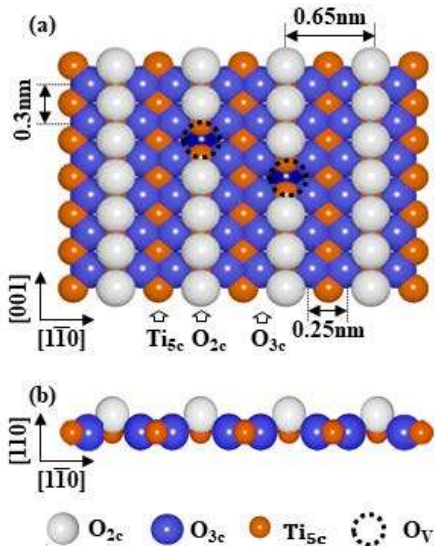


**Figure 1.** A ball model of the rutile $TiO_2(110)$-1×1 surface; (a) top view, and (b) side view. $O_{2c}$ (white balls): two-fold coordinated bridge oxygen row; $O_{3c}$ (blue balls): in plane three-fold coordinated oxygen; $Ti_{5c}$ (orange balls): rows of five-fold coordinated Ti atoms; $O_V$ (black dotted circles): oxygen vacancy.

The dissociation pattern of oxygen molecules on the reduced rutile $TiO_2(110)$ surface at low temperatures has been fairly well understood[30,31,36,37]. Usually, $O_v$ acts as the most abundant surface electron donor and hence the most favorable adsorption site for the oxygen, as proposed in several experimental works[31,34,35] and theoretical simulations[36-38]. A typical nc-AFM image of the reduced rutile $TiO_2(110)$-1×1 surface measured in the hole mode (positively charged tip apex) featuring $O_v$ defects is presented in Figure S2. Moreover, it has been proposed that the $Ti_{int}$ defects in the near surface region play dominant role in the dissociation and charge state of the adsorbed $O_{ad}$.[25,28] Dosing molecular oxygen on a reduced rutile $TiO_2(110)$ surface positions the lowest unoccupied molecular orbital (LUMO) below the Fermi level ($E_F$) of the reduced $TiO_2(110)$ substrate[21]. This causes both spontaneous charging of the adsorbed oxygen molecules by the itinerant electrons from pre-existing defects and $O_2$ dissociation into two $O_{ad}$. Recently, two $O_{ad}$ adsorption and dissociation channels on rutile $TiO_2(110)$-1×1 surface have been proposed by an experimental and theoretical study[38] (for further details, see Figure S3). However, the charge state of the $O_{ad}$ adsorbed on the partially reduced substrate will strongly depend on the distribution of electron donors[39] in the near-surface region, especially on the inhomogeneous concentration of the $Ti_{int}$[25,28,35]. Under high annealing temperature (> 400 K), the $Ti_{int}$ can diffuse from the bulk to the near-surface region via an interstitial diffusion mechanism[25]. With a relatively significant migration energy barrier (about ~ 1 eV), the concentration and distribution of $Ti_{int}$ in the near-surface region can vary significantly, depending on the level of bulk reduction[25].

Here, we have, for the first time, successfully measured and manipulated the charge state of the $O_{ad}$ adsorbed on the reduced rutile $TiO_2(110)$-1×1 surface using a combined system of home-built nc-AFM and Kelvin probe force microscopy (KPFM) at 78 K. In particular, we managed to clearly distinguish the differently charged single and double $O_{ad}$ in AFM and KPFM images and assign them to $O_{ad}^-$ (or $2O_{ad}^-$), $O_{ad}^{2-}$ or $(2O_{ad}^{2-})$ and $O_{ad}^-$-$O_{ad}^{2-}$ species, respectively. These charged oxygen species are formed by transferring nominally one or two electrons to a local region around the adsorbed $O_{ad}$ from the inhomogeneously distributed electron donors. This assignment is consistent with the appreciably stronger attractive force and larger $V_{LCPD}$ obtained on the $O_{ad}^{2-}$ compared to the $O_{ad}^-$. Furthermore, in addition to our ability to distinguish the charge states of the adsorbed $O_{ad}$, we also demonstrate our ability to deliberately and reversibly manipulate the charge states between $O_{ad}^-$ and $O_{ad}^{2-}$ by changing the frequency shift set point (effectively, the tip height). The charge state transitions can be understood as arising from the tip-induced shifts of the electronic levels of the adsorbates due to inhomogeneous electric field modulated by the tip-sample distance. The experimental phenomena are analyzed by schematic energy models in combination with band-bending theory and density functional theory (DFT) simulations.

EXPERIMENTAL SECTION

**Experimental methods** Home-built combined nc-AFM and KPFM system was used to measure and manipulate the charge state of the adsorbed $O_{ad}$ on reduced rutile $TiO_2(110)$-1×1 surface (the thermodynamically most stable facet) under ultrahigh vacuum conditions (base pressure below $5 \times 10^{-11}$ Torr) at 78 K. The nc-AFM was operated in a frequency-modulation mode with an iridium-coated Si cantilever used as a sensor with small oscillation amplitude (5 Å). A bias voltage was applied to the sample. The nc-AFM images were obtained in the constant-frequency shift ($\Delta f$) mode and the KPFM images were recorded with a bias voltage feedback in the constant-height mode. All spectra on the target $O_{ad}$ were measured with the atom tracking technique[46]. The tip and sample were treated by cycles of Ar ion sputtering and annealing. After that, the clean sample was exposed to oxygen gas of high purity (99.9 %) at room temperature and then the sample was characterized at 78 K. Additional experimental details are presented in Supporting Information (SI).

**DFT simulations** Our calculations were performed in the slab geometry with 3D periodic boundary conditions. The surface was modeled using a six-layer stoichiometric $TiO_2$ rutile slab. In the $z$ direction, the slabs were separated from their periodic images by 15Å vacuum gap, see the SI for details. Calculations of the energies and forces were performed using DFT with projector augmented-wave pseudopotentials[47] along with the hybrid HSE06 exchange-correlation functional[48] and 400 eV plane wave cutoff as implemented in the VASP code[49]. The HSE06 functional was selected since the GGA treatment was unable to ensure localization of polarons and stabilize the $O_{ad}^-$-$O_{ad}^{2-}$ configurations. Ionic forces were converged to the accuracy better than 0.01 eV/Å.

An experimental procedure of charging of the oxygen adatoms by the tip was in practice modeled by directly adding/removing electrons to/from the oxygen adatoms in the following way. In experiments the charge transferred to the molecule has

two possible sources: the tip and the substrate defects. In order to avoid complications of dealing with charged systems in a periodic setup, we ignore the tip and model the electron reservoir by providing, as an artificial device, O-H or $O_v$ defects in our simulation cell, see the SI, which leads to localized polarons somewhere within the slab. The charge trapped in the polarons is released to oxygen species either spontaneously or manually by preparing slight structural deviations from the relaxed local polaron geometry prior to relaxation of the whole system. Details of this procedure are described in SI. This procedure captures correctly the major processes leading to charging of the oxygen adatoms, but ignores much smaller accompanying dipole interactions formed in the process of charging. In order to doubly charge two oxygen adatoms as done experimentally, we provide four electrons either from two $O_v$ or four OH donor defects built in our model, which leave electrons behind in the Ti $d$ orbitals[52]. The same effect could have been achieved by considering the $Ti_{int}$ interstitials which we argue elsewhere are in fact the dominant defects.

Bader analysis[53] of the formal charges was also performed, for details see SI. In order to couple the simulations directly to the experimentally measured images, constant height images have been calculated. Assuming relatively large tip-surface distances $z$, only the local surface electrostatic potential $U_{loc}(z)$ is used to simulate the nc-AFM images. This approach ignores completely the large van der Waals (vdW) interaction and also the presumably much smaller exchange-correlation effects. In this approximation the tip force $F_{ts}(z) = -\frac{d}{dz}U_{loc}(z)$, while the frequency shift was obtained as[54]

$$\Delta f(d) \propto \int_0^{2\pi} F_{ts}(d + A\cos\varphi)\cos\varphi \, d\varphi.$$

This model is relevant to the hole mode imaging used in the experiments and corresponds to a point charge oscillating at a distance $d$ with amplitude $A$; we have used $d = 7$Å and $A = 4$ Å.

RESULTS AND DISCUSSION

A representative atomic-scale nc-AFM image of the O−TiO$_2$(110)-1×1 surface is shown in Figure 2(a). Here, the dark and bright rows correspond to the alternating five-fold coordinated titanium rows ($Ti_{5c}$) and two-fold coordinated bridge oxygen rows ($O_{2c}$), respectively, see also Figure 1. Several types of oxygen species on $Ti_{5c}$ rows are clearly visible as bright spots with different contrast. The line profiles through two oxygen species of different contrast are shown in Figures 2(c,d). Note that precise quantification of the charge localized on each oxygen adatom represents an experimental challenge. We assign the faint single and double spots to $O_{ad}^-$ and $2O_{ad}^-$, and the pronounced single and double spots to $O_{ad}^{2-}$ and $2O_{ad}^{2-}$, respectively. The characterization of the charge state of the $O_{ad}$ is performed at a relatively large tip-sample distance to avoid the tip effect. As explained in Figure S3, the fact that the double oxygen adatoms are much more abundant than the single ones indicates that the adsorbed oxygen species are primarily dissociated by a non-vacancy mechanism and suggests that the $Ti_{int}$ rather than $O_v$ are the dominant defects. Comparison with calculated Bader charge analysis[53], Table S1, suggests that the charges of the $O_{ad}^{2-}$ and $O_{ad}^-$ are only 0.75 and 0.45 electrons, respectively, i.e. appreciably smaller than the formal charges. This is due to the charge transferred to the other nearby surface oxygen atoms,

see Figure S11. We also find that the $O_{ad}^{2-}$ and $2O_{ad}^{2-}$ are the distinctly dominant species with a coverage of 0.078 ML (1 ML $= 5.2 \times 10^{14}$/cm$^2$), as compared to the $O_{ad}^-$ and $2O_{ad}^-$ (0.013 ML). This is in line with the computed relative energies of 2.66/0.96/0.0 eV for the $2O_{ad}^-$, $O_{ad}^- - O_{ad}^{2-}$, and $2O_{ad}^{2-}$ states shown in Figure 2(b), hence favoring the $2O_{ad}^{2-}$ state over the $2O_{ad}^-$ state by 2.66 eV. The $2O_{ad}^-$, $O_{ad}^- - O_{ad}^{2-}$ states are local (meta)stable minima with expected sufficiently long lifetimes at 78K. We interpret the presence of these experimentally observed high-energy states at low temperature by local shortage of the polaronic defects, which would otherwise charge them to an energetically more favorable $2O_{ad}^{2-}$ state. In addition, most adsorbed $O_{ad}$, whether in $2O_{ad}^-$ or $2O_{ad}^{2-}$ states, maintain their configurations as a pair of adjacent $O_{ad}$ along the $Ti_{5c}$ rows, which is in good agreement with the high dissociation energy barriers[31]. Calculations show that these fully dissociated kinetically hindered states with the two adsorbed $O_{ad}^{2-}$ at the second-neighbor lattice distance are ≈0.7 eV lower in energy. Furthermore, it was suggested that the excess charge on these adjacent pairs of $O_{ad}$ is provided primarily by the $Ti_{int}$[25]. Although challenges exist in directly characterizing the $Ti_{int}$, the formation of fresh TiO$_x$ islands[25,35] and the observed adsorbed adjacent $O_{ad}$ pair configuration provide an indirect indication that the $Ti_{int}$ rather than $O_v$ plays a dominant role in determining the adsorption behavior and the nature of the charge state of the $O_{ad}$.
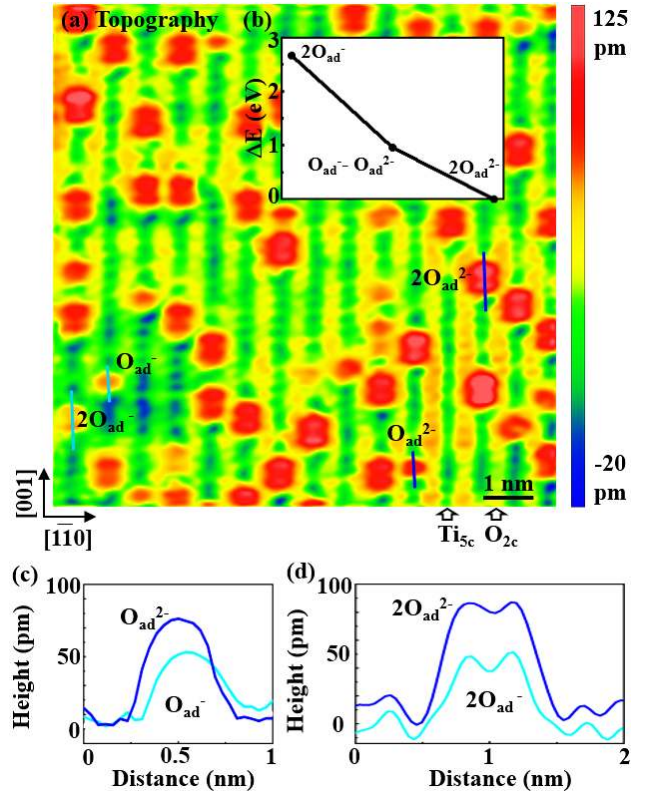
**Figure 2.** (a) Constant-$\Delta f$ AFM image (hole mode, 10×10 nm$^2$) of O−rich TiO$_2$(110)-1×1 surface. $O_{2c}$: two-fold coordinated bridge oxygen rows. $Ti_{5c}$: five-fold coordinated titanium rows. $O_{ad}^-/2O_{ad}^-$ (0.013 ML) and $O_{ad}^{2-}/2O_{ad}^{2-}$ (0.078 ML): single/double oxygen adatoms on $Ti_{5c}$ rows in different charge states. Imaging parameters: $f_0 = 816$ kHz, $A = 500$ pm, $Q = 13600$, $T = 78$ K, $\Delta f = -450$ Hz, $V = +1.05$ V. (b) DFT computed energies of

3

$2O_{ad}^-$, $O_{ad}^- - O_{ad}^{2-}$, and $2O_{ad}^{2-}$ states; (c) and (d) corresponding line profiles as indicated in (a).

In Figure 3 we show the frequency shift ($\Delta f$) and local contact potential difference ($V_{LCPD}$) images of the oxygen species on $O-TiO_2(110)$-1×1 surface measured simultaneously in the constant−height mode. A schematic of the measurement circuit of frequency−modulation KPFM (FM-KPFM) with bias voltage feedback is shown in Figure S1. As shown in Figures 3(a-c), we have obtained several different contrast patterns of the oxygen adatom species on the $Ti_{5c}$ rows, which we assign to $2O_{ad}^-$ and $2O_{ad}^{2-}$, respectively, see also the large scan area in Figure S4. Besides that, we also observe $O_{ad}^- - O_{ad}^{2-}$ species which, compared to $2O_{ad}^-$, are theoretically predicted to be energetically much more favorable. The DFT simulated $|\Delta f|$ images of $2O_{ad}^{2-}$, $2O_{ad}^-$ and $O_{ad}^- - O_{ad}^{2-}$ species are presented in Figures 3(d-f), respectively. These computed images exhibit excellent agreement with the measured images. The simulations also suggest that the configuration with the $p$-orbitals rotated from the main $[1\bar{1}0]$ axis is one of several quasi-degenerate local minima the system may adopt. And indeed, the experiment/theory comparison strongly suggests a subatomic experimental resolution as rotated oxygen $p$-orbitals of the $2O_{ad}^-$ species are imaged as shown in Figures 3(b,e), for more details, see SI. The corresponding line profiles are shown in Figures 3(j,k). We found that $2O_{ad}^{2-}$, compared to $2O_{ad}^-$, yields significantly larger absolute values of the $\Delta f$ and $V_{LCPD}$, indicating a larger charge, in perfect agreement with the findings in Figure 2. In contrast, the "sizes" of the three oxygen species are broadly similar, both experimentally and from the simulations, making their identification solely by size impossible.
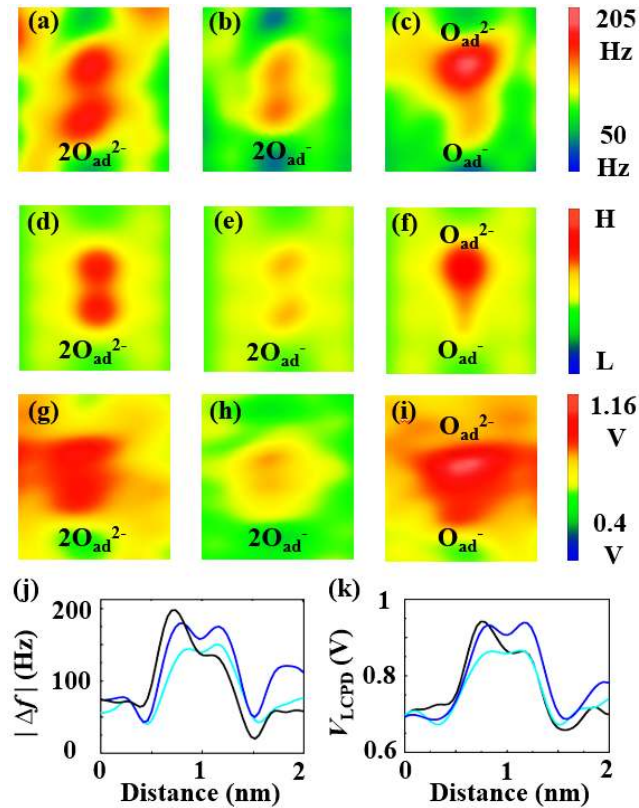


(a) 2$O_{ad}^{2-}$ (b) 2$O_{ad}^-$ (c) $O_{ad}^{2-}$ $O_{ad}^-$ 205 Hz / 50 Hz

(d) 2$O_{ad}^{2-}$ (e) 2$O_{ad}^-$ (f) $O_{ad}^{2-}$ $O_{ad}^-$ H / L

(g) 2$O_{ad}^{2-}$ (h) 2$O_{ad}^-$ (i) $O_{ad}^{2-}$ $O_{ad}^-$ 1.16 V / 0.4 V

(j) (k)

**Figure 3.** (a-c) Experimental (constant-height mode, 0.7×1.5 $nm^2$) and (d-f) simulated $|\Delta f|$ images of $2O_{ad}^{2-}$, $2O_{ad}^-$ and $O_{ad}^- - O_{ad}^{2-}$ species on O−rich $TiO_2(110)$-1×1 surface, respectively. (g-i) Local contact potential difference ($V_{LCPD}$) image of the same area as in (a-c). (j) and (k) Corresponding line profiles of $|\Delta f|$ and $V_{LCPD}$ though $2O_{ad}^{2-}$ (blue), $2O_{ad}^-$ (cyan) and $O_{ad}^- - O_{ad}^{2-}$ (black) sites taken along the centers of both atoms in the images, as indicated in Figures S4(a,b). Imaging parameters: $f_0$ = 816 kHz, $A$ = 500 pm, $Q$ = 13600, $T$ = 78 K, $\Delta f$ = -320 Hz.

The strong difference in contrast of the differently charged oxygen species seen in the AFM images is customarily attributed to the different short-range force ($F_{SR}$) resulting from the charge state. In order to pursue this concept further, we show in Figure 4(a) the $F_{SR}$ measured on these two species. We find that the maximum attractive force on the $O_{ad}^{2-}$ is appreciably larger than that on $O_{ad}^-$, a finding which is again consistent with the experimental results in Figure 2. We note that during spectra measurement we employed the atom tracking-technique to counteract the thermal drift effects[46]. After spectra measurements, the same spots attributed to $O_{ad}$ were characterized again to verify that no unexpected manipulation of the adsorbed $O_{ad}$ by the AFM tip happened, such as a charge state switching or lateral position displacement (see Figure S4).
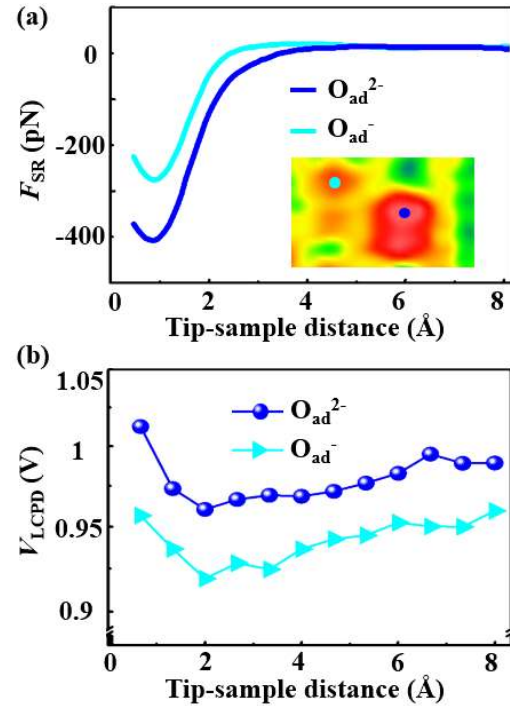


**Figure 4.** (a) Short-range force ($F_{SR}$) and (b) $V_{LCPD}$ curves above $O_{ad}^-$ and $O_{ad}^{2-}$ sites (as shown in the inset in (a)). An atom tracking technique is employed to overcome the thermal drift during measurements. Imaging parameters: $f_0$ = 816 kHz, $A$ = 500 pm, $Q$ = 13600, $T$ = 78 K, $\Delta f$ = -350 Hz.

We have further investigated the charge states on the oxygen adatoms and their effect on the $V_{LCPD}$ by performing Kelvin probe force spectroscopy (KPFS) as a function of the tip-sample

4

distance ensuring that no tip changes or manipulation of the target $O_{ad}$ could occur. By fitting each $\Delta f\,(V)$ to a parabola at a given tip-sample distance, the peak positions are determined, yielding $V_{LCPD}$. Quantitatively, the $V_{LCPD}$ values are affected by many factors, such as the tip termination and polarity. As shown in Figure 4(b), the trend we observe within the measurement range is that the $V_{LCPD}$ values on $O_{ad}^{2-}$ sites are always larger than those on $O_{ad}^{-}$ sites. We attribute this systematic trend of shift of $V_{LCPD}$ values to the potential difference of the differently charged $O_{ad}$ induced by accumulation of more charge on the $O_{ad}^{2-}$ sites compared to the $O_{ad}^{-}$ sites, resulting in larger $V_{LCPD}$ values. On the other hand, the variation of $V_{LCPD}$ values with tip height directly indicates a change of band bending of the semiconductor substrate[21,55]. The experimental measurements demonstrate that the charge states of the adsorbed $O_{ad}$ can be clearly distinguished and determined due to the strong (subatomic) image contrast of nc-AFM and KPFM.

Our experiments, corroborated by computed energies, clearly suggest that $O_{ad}^{2-}$ and $2O_{ad}^{2-}$ are ground state configurations whereas $O_{ad}^{-}$, $2O_{ad}^{-}$, and $O_{ad}-O_{ad}^{2-}$ are local minima (metastable) charge configurations kinetically stabilized at the low temperature used here. Therefore, in line with the previous related work[3,8,9,21,22], which proved applicability of the nc-AFM to controlled manipulation of the charge states of adsorbed atoms and molecules, we explore now the nc-AFM tip as a tool for the charge state manipulation of the adsorbed $O_{ad}$.
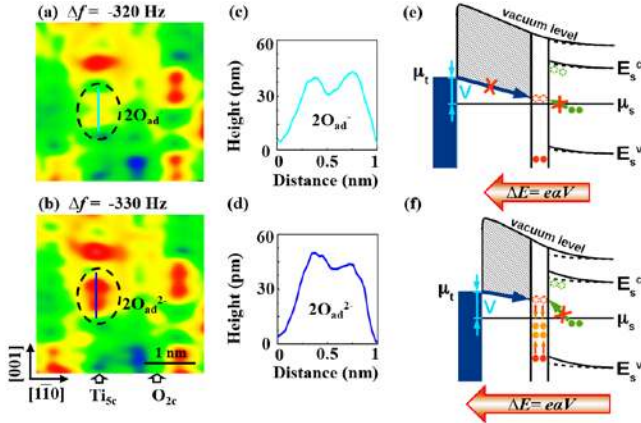


**Figure 5.** (a) and (b) Constant-$\Delta f$ AFM images of the charging process of the adsorbed oxygen adatoms by the AFM tip. (c) and (d) The corresponding line profiles of the target $2O_{ad}^{-}$ and $2O_{ad}^{2-}$ species labeled by dashed black ovals in (a) and (b). (e) and (f) The corresponding schematic models showing the key electronic energy levels and tunneling barriers responsible for the charging process. $e$, elementary charge; $\alpha$, level arm; $V$, bias voltage. Occupied/unoccupied states of oxygen electrons (full/empty dashed circles) are depicted in orange/red for $2O_{ad}^{2-}$/$2O_{ad}^{-}$. Occupied/unoccupied polaronic states (full/empty dashed circles) are depicted in green, the tip states in blue. $\mu_t$ and $\mu_s$ are the Fermi energies of the tip and surface, $E_s^v$ and $E_s^c$ are the top and the bottom of the surface valence and conduction bands, respectively. The band bending shown by dashed lines corresponds to the oxygen adsorption and to the total bending that includes also the metal-semiconductor contact bias induced field effect by full lines. The arrows indicate the repositioning

of the respective levels in energy, the crosses the inhibited processes. The indicated trends follow from DFT calculations shown in Figure S10. Imaging parameters: (a) $\Delta f$ = -320 Hz, $V$ = +1.05 V; (b) $\Delta f$ = -330 Hz, $V$ = +1.05 V.

Figure 5 shows a charging process of the adsorbed oxygen adatoms induced by a modification of the frequency shift (set point) under a fixed applied positive bias voltage (see also charging of oxygen species by increasing bias voltage in Figure S6). In Figure 5(a), an oxygen adatom pair indicated by a dashed black oval is imaged as a couple of weak contrast spots and accordingly assigned to the $2O_{ad}^{-}$ species. By gradually increasing the frequency shift upon decreasing the tip-sample distance with applied constant bias voltage of +1.05 V, the species is pairwise charged to $2O_{ad}^{2-}$ (two spots with strong contrast), Figure 5(b). To shed more light, we show in Figures 5(c,d) the corresponding line profiles which corroborate the above assignments. The underlying charging mechanism is explained in Figures 5(e,f) showing the schematics of the shifts of the key electronic energy levels and modification of the tunneling barrier. Here, the charging process is attributed[8,9] to the gradually enhanced tip-induced electric field $E$, which results in the electron transfer from the nc-AFM tip to the adsorbed oxygen species. The magnitude of the energy shift, $\Delta E$, induced by the applied electric field, $E$, can be modeled as[9]:

$$\Delta E = e\alpha V,$$

where $\alpha$ is the so-called level arm which is inversely proportional to the tip-sample distance $d$. With a constant $V$, the $\Delta E$ only depends on $d$. As discussed above, the metastable adsorbed $O_{ad}^{-}$ and $2O_{ad}^{-}$ are kinetically hindered being kept at equilibrium with the polarons. By gradually increasing $\Delta E$, the $E$ can induce electron tunneling through the vacuum gap and electron injection to the adsorbed $2O_{ad}^{-}$ when the threshold electric field, $E_{th}$, is reached. As a result, the adsorbed $2O_{ad}^{-}$ is charged to $2O_{ad}^{2-}$. During the charge state transition, the unoccupied level of the singly charged oxygen species is gradually raised up accompanying by further upward band bending[55]. After the formation of $2O_{ad}^{2-}$, a fully charged oxygen species is formed, thus hindering further electron injection from the AFM tip. This also suggests that the $O_{ad}^{2-}$/$2O_{ad}^{2-}$ species are the most stable states, which is consistent with the dominant species observed in Figure 2(a) as well as with the computed energies of the different charge states, Figure 2(b).

After having demonstrated the ability to charge the adsorbed $2O_{ad}^{-}$ species to $2O_{ad}^{2-}$ by reducing the tip height, we now demonstrate also a more complicated process of a reversible discharging/recharging of the adsorbed oxygen adatom simply by a continuous reduction of the tip-sample distance, $d$, while keeping the same voltage. The process is demonstrated in Figure 6. In the charge state transition regime, one of the two $O_{ad}^{2-}$ atoms in Figure 6(a) is discharged to $O_{ad}^{-}$, Figure 6(b), and recharged again to $O_{ad}^{2-}$, Figure 6(c), simply by controlling the tip-sample distance $d$ and hence the electric field $E$. For clarity, the corresponding line profiles of the reference and target $O_{ad}$ pairs are shown in Figures 6(d,f). The models showing the schematic of the key electronic energy levels and tunneling barriers are given in Figures 6(g-i). We speculate that in the discharging process, from (a) to (b), the enhanced field, $E$, will result in an electron transfer from the $O_{ad}^{2-}$ to the substrate as a polaron. Meanwhile, the singly occupied $O_{ad}^{-}$ state is formed and lifted

5

upwards in energy by the tip. As expected, by further decreasing the tip-sample distance, $d$, electron tunneling probability increases, resulting in the tunneling of an electron from the AFM tip back into the discharged $O_{ad}^-$. The $O_{ad}^{2-}$ species is recreated as presented in Figure 6(c,i). The model outlined in Figures 6(g-i) assumes discharging into a polaron as explicitly built in our computational model (e). In reality, as also suggested by Figures 6(a,b), instead of charging a polaron, the charge may be transferred to the nearby $O_{ad}^-$ atom which has an energy level close to the polaronic levels. Surprisingly, in addition to the reversible discharging and recharging transitions, some unexpected phenomena are observed as well. For example, the other atom $O_{ad}^{2-}$ of the pair maintains stability during the charge state switching of the target $O_{ad}^{2-}$. We interpret this finding by a shortage of states available for draining charge. Supplementary Figure S5 shows other examples when under experimentally identical conditions the manipulation of another species does not occur. This is in line with experimental observations on charge manipulation of oxygen molecules on the anatase $TiO_2$ surface[21].
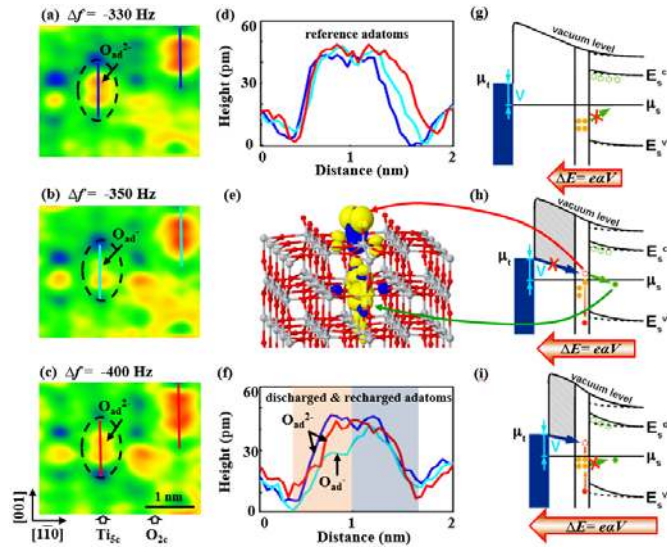


**Figure 6.** Constant-$\Delta f$ AFM images of (a) $2O_{ad}^{2-}$, (b) $O_{ad}^- - O_{ad}^{2-}$ and (c) $2O_{ad}^{2-}$ species. (e) Calculated magnetization (spin density) depicting an empty $O_{ad}^-$ orbital along with a subsurface polaron (yellow/blue). (d), (f) Line profiles corresponding to reference and target $O_{ad}$ species as indicated by the same colors in (a-c). (e) Calculated spin density of the $O_{ad}^- - O_{ad}^{2-}$ species. (g-i) Corresponding schematic models showing the key electronic energy levels and tunneling barriers responsible for the charging process. The same notations are used as in Figure 5. Imaging parameters: (a) $\Delta f$ = -330 Hz, $V$ = +1.05 V; (b) $\Delta f$ = -350 Hz, $V$ = +1.05 V; (c) $\Delta f$ = -400 Hz, $V$ = +1.05 V.

## CONCLUSIONS

In conclusion, we have investigated the charge states of the adsorbed single and double oxygen atoms adsorbed on the rutile $TiO_2(110)$-1×1 surface by nc-AFM and KPFM at 78K in ultra-high vacuum. We managed to clearly identify with atomic/sub-atomic resolution the differently charged single and double oxygen adatoms as $O_{ad}^-/2O_{ad}^-$, $O_{ad}^{2-}/2O_{ad}^{2-}$ and $O_{ad}^- - O_{ad}^{2-}$ species, respectively, combining the measurement of $F_{SR}$ and $V_{LCPD}$ as a

function of the tip-sample distance and extensive DFT simulations. $O_{ad}^-/2O_{ad}^-$ and $O_{ad}^- - O_{ad}^{2-}$ species are metastable but can still be observed at low temperatures despite their formation energies being up to $\approx$ 3 eV higher than the ground state $O_{ad}^{2-}/2O_{ad}^{2-}$ species. Comparison with DFT simulations reveals that the charge transferred to/from the adatoms is smaller than the nominal charge, due, in part, to the fact that charge is spread over other nearby surface oxygen atoms. In addition to determining the charge states of the oxygen adatoms, we also succeeded in deliberately charging and discharging, individually and pairwise, the oxygen adatoms by the nc-AFM tip by means of gradually decreasing the tip-sample distance, while keeping the sample at a fixed positive voltage. The fact that both charging and discharging processes do occur at constant voltage suggests an activation of different processes due to modulating the tip-induced electric field. We argue that the charging processes involve electron tunneling from the tip into the oxygen adatom $p$-states while the discharging process proceeds by draining the charge into polarons or other nearby oxygen adatoms, which all are close in energy. For that reason, manipulation of other adatoms on different parts of the surface may not be possible under otherwise identical experimental conditions due to local shortage of states available for the discharge. The polarons abundant on the rutile $TiO_2(110)$ surface play a vital role in the processes studied. In that respect, the importance of the bulk interstitial defects, $Ti_{int}$, was particularly emphasized. Our study shows a novel route for the measurement and manipulation of the charge states of the adsorbates at the atomic scale and opens a door for further investigation of electronic devices and catalytic reactions based on single atoms.

## ASSOCIATED CONTENT

### Supporting Information

Experimental details and schematic circuits of FM-KPFM with bias voltage feedback; typical AFM image and corresponding ball model of rutile $TiO_2(110)$-1×1 surface in the hole mode; ball models of the two proposed adsorption and dissociation types of oxygen adatoms on rutile $TiO_2(110)$ surface; stable $2O_{ad}^-$, $2O_{ad}^{2-}$ species after spectra measurement; charging the adsorbed oxygen species by increasing the bias voltage. Further simulation details, such as the geometry, including of the polarons, preparation of desired oxygen charge states in the simulations, subatomic resolution, Bader analysis of computed charges on the oxygen species, effect of the electric field on the key electronic states and charge distributions corresponding to different charging.

## AUTHOR INFORMATION

### Corresponding Author

*liyanjun@ap.eng.osaka-u.ac.jp

### ORCID

Ivan Štich:  0000-0003-3338-8737

Ján Brndiar: 0000-0002-2016-3216

Lev Kantorovich: 0000-0001-9379-6834

Yan Jun Li: 0000-0001-7845-326X

Huan Fei Wen: 0000-0002-2972-9669

REFERENCES

(1) Costas, M.; Mehn, M. P.; Jensen, M. P.; Que, L. *Chem. Rev.* **2004**, *104*, 939.

(2) Olsson, F. E.; Paavilainen, S.; Persson, M.; Repp, J.; Meyer, G. *Phys. Rev. Lett.* **2007**, *98*, 176803.

(3) Gross, L.; Mohn, F.; Liljeroth, P.; Repp, J.; Giessibl, F. J.; Meyer, G. *Science* **2009**. *324*, 1428.

(4) Steurer, W.; Repp, J.; Gross, L.; Scivetti, I.; Persson, M.; Meyer, G. *Phys. Rev. Lett.* **2015**, *114*, 036801.

(5) Repp, J.; Meyer, G.; Olsson, F. E.; Persson, M. *Science* **2004**, *305*, 493.

(6) Sterrer, M.; Risse, T.; Pozzoni, U. M.; Giordano, L.; Heyde, M.; Rust, H. P.; Pacchioni, G.; Freund, H. J. *Phys. Rev. Lett.* **2007**, *98*, 096107.

(7) Swart, I.; Sonnleitner, T.; Repp, J. *Nano Lett.* **2011**, *11*, 1580.

(8) Rahe, P.; Steele, R. P.; Williams, C. C. *Nano Lett.* **2016**, *16*, 911.

(9) Kocić, N.; Weiderer, P.; Keller, S.; Decurtins, S.; Liu, S. X.; Repp, J. *Nano Lett.* **2015**, *15*, 4406.

(10) Fernández-Torrente, I.; Kreikemeyer-Lorenzo, D.; Stróżecka, A.; Franke, K. J.; Pascual, J. I. *Phys. Rev. Lett.* **2012**, *108*, 036801.

(11) Fu, Y. S.; Zhang, T.; Ji, S. H.; Chen, X.; Ma, X. C.; Jia, J. F.; Xue, Q. K. *Phys. Rev. Lett.* **2009**, *103*, 257202.

(12) Wu, S. W.; Ogawa, N.; Ho, W. *Science* **2006**, *312*, 1362.

(13) Marczinowski, F.; Wiebe, J.; Meier, F.; Hashimoto, K.; Wiesendanger, R. *Phys. Rev. B* **2008**, *77*, 115318.

(14) Zaknoon, B.; Bahir, G.; Saguy, C.; Edrei, R.; Hoffman, A.; Rao, R.A.; Muralidhar, R.; Chang, K. M. *Nano Lett.* **2008**, *8*, 1689.

(15) Hummon, M. R.; Stollenwerk, A. J.; Narayanamurti, V.; Anikeeva, P. O.; Panzer, M. J.; Wood, V.; Bulović, V. *Phys. Rev. B* **2010**, *81*, 115439.

(16) Teichmann, K.; Wenderoth, M.; Loth, S.; Ulbrich, R. G.; Garleff, J. K.; Wijnheijmer, A. P.; Koenraad, P.M. *Phys. Rev. Lett.* **2008**, *101*, 076103.

(17) Song, C. L.; Jiang, Y. P.; Wang, Y. L.; Li, Z.; Wang, L.; He, K.; Chen, X.; Ma, X. C.; Xue, Q. K. *Phys. Rev. B* **2012**, *86*, 045441.

(18) Cui, Y.; Nilius, N.; Freund, H. J.; Prada, S.; Giordano, L.; Pacchioni, G. *Phys. Rev. B* **2013**, *88*, 205421.

(19) Wen, H. F.; Li, Y. J.; Arima, E.; Naitoh, Y.; Sugawara, Y.; Xu, R.; Cheng, Z. H. *Nanotechnology* **2017**, *28*, 105704.

(20) Kou, L.; Li, Y. J.; Kamijyo, T.; Naitoh, Y.; Sugawara, Y. *Nanotechnology* **2016**, *27*, 505704.

(21) Setvin, M.; Hulva, J.; Parkinson, G. S.; Schmid, M.; Diebold, U. *Proc. Natl. Acad. Sci.* **2017**, *114*, E2556.

(22) Steurer, W.; Fatayer, S.; Gross, L.; Meyer, G. *Nat. Commun.* **2015**, *6*, 8353.

(23) Sugimoto, Y.; Abe, M.; Hirayama, S.; Oyabu, N.; Custance, Ó.; Morita, S. *Nat. Mater.* **2005**, *4*, 156.

(24) Sugimoto, Y.; Pou, P.; Custance, O.; Jelinek, P.; Abe, M.; Perez, R.; Morita, S. *Science* **2008**, *322*, 413.

(25) Wendt, S.; Sprunger, P. T.; Lira, E.; Madsen, G. K.; Li, Z.; Hansen, J. Ø.; Matthiesen, J.; Blekinge-Rasmussen, A.; Lægsgaard, E.; Hammer, B.; Besenbacher, F. *Science* **2008**, *320*, 1755.

(26) Wahlström, E.; Vestergaard, E. K.; Schaub, R.; Rønnau, A.; Vestergaard, M.; Lægsgaard, E.; Stensgaard, I.; Besenbacher, F. *Science* **2004**, *303*, 511.

(27) Matthiesen, J.; Wendt, S.; Hansen, J.Ø.; Madsen, G. K.; Lira, E.; Galliker, P.; Vestergaard, E. K.; Schaub, R.; Lægsgaard, E.; Hammer, B.; Besenbacher, F. *ACS Nano* **2009**, *3*, 517.

(28) Lira, E.; Wendt, S.; Huo, P.; Hansen, J. Ø.; Streber, R.; Porsgaard, S.; Wei, Y.; Bechstein, R.; Lægsgaard, E.; Besenbacher, F. *J. Am. Chem. Soc.* **2011**, *133*, 6529.

(29) Tan, S.; Ji, Y.; Zhao, Y.; Zhao, A.; Wang, B.; Yang, J.; Hou, J. G. *J. Am. Chem. Soc.* **2011**, *133*, 2002.

(30) Wang, Z. T.; Deskins, N. A.; Lyubinetsky, I. *J. Phys. Chem. Lett.* **2011**, *3*, 102.

(31) Du, Y.; Deskins, N. A.; Zhang, Z.; Dohnalek, Z.; Dupuis, M.; Lyubinetsky, I. *Phys. Chem. Chem. Phys.* **2010**, *12*, 6337.

(32) Petrik, N. G.; Kimmel, G. A. *J. Phys. Chem. Lett.* **2010**, *1*, 1758.

(33) Wang, Z. T.; Du, Y.; Dohnálek, Z.; Lyubinetsky, I. *J. Phys. Chem. Lett.* **2010**, *1*, 3524-3529.

(34) Du, Y.; Dohnalek, Z.; Lyubinetsky, I. *J. Phys. Chem. C* **2008**, *112*, 2649.

(35) Zhang, Z.; Lee, J.; Yates Jr, J. T.; Bechstein, R.; Lira, E.; Hansen, J. Ø.; Wendt, S.; Besenbacher, F. *J. Phys. Chem. C* **2010**, *114*, 3059.

(36) Xu, H.; Tong, S. Y. *Surf. Sci.* **2013**, *610*, 33.

(37) Rasmussen, M. D.; Molina, L. M.; Hammer, B. *J. Chem. Phys.* **2004**, *120*, 988.

(38) Lira, E.; Hansen, J. Ø.; Huo, P.; Bechstein, R.; Galliker, P.; Lægsgaard, E.; Hammer, B.; Wendt, S.; Besenbacher, F. *Surf. Sci.* **2010**, *604*, 1945.

(39) Li, Y. F.; Selloni, A. *J. Am. Chem. Soc.* **2013**, *135*, 9195.

(40) Deskins, N. A.; Rousseau, R.; Dupuis, M. *J. Phys. Chem. C* **2010**, *114*, 5891-5897.

(41) Wang, Y.; Pillay, D.; Hwang, G. S. *Phys. Rev. B* **2004**, *70*, 193410.

(42) Wu, X.; Selloni, A.; Lazzeri, M.; Nayak, S. K. *Phys. Rev. B* **2003**, *68*, 241402.

(43) Lu, G.; Linsebigler, A.; Yates Jr, J. T. *J. Chem. Phys.* **1995**, *102*, 3005.

(44) de Lara-Castells, M. P.; Krause, J. L. *Chem. Phys. Lett.* **2002**,*354*, 483.

(45) Scanlon, D. O.; Dunnill, C. W.; Buckeridge, J.; Shevlin, S. A.; Logsdail, A. J.; Woodley, S. M.; Catlow, C. R. A.; Powell, M. J.; Palgrave, R. G.; Parkin, I. P.; Watson, G. W. *Nat. Mater.* **2013**, *12*, 798.

(46) Sawada, D.; Sugimoto, Y.; Morita, K. I.; Abe, M.; Morita, S. *Appl. Phys. Lett.* **2009**, *94*, 173117.

(47) Blöchl, P. E. *Phys.* **1994**, *50*, 17953.

(48) Krukau, A. V.; Vydrov, O. A.; Izmaylov, A. F.; Scuseria, G. E. J. Chem. Phys. **2006***, 125, 224106.*

(49) Kresse, G.; Furthmüller, J. *Comput. Mater. Sci.* **1996**, *6*, 15.

(50) Perdew; J. P.; Burke. K.; Ernzerhof, M. *Phys. Rev. Lett.* **1996**, *77*, 3865.

(51) Dudarev, S. L.; Botton, G. A.; Savrasov, S. Y.; Humphreys C. J.; Sutton, A. P. *Phys. Rev.* **1998** *B 57,* 1505.

(52) Deskins, N. A.; Rousseau, R.; Dupuis, M. *J. Phys. Chem.,* **2011**, *C 115,* 7562.

(53) Bader, R. F. W., *Atoms in Molecules - A quantum theory*, Oxford University Press, New York, 1990.

(54) Giessibl, F. J. *Rev. Mod. Phys.* **2003**, 75, 949.

(55) Zhang, Z.; Yates Jr, J. T. *Chem. Rev.* **2012**, *112*, 5520.

Table of contents graphic: